Photochemistry and Spectroscopy
https://www.sciltp.com/journals/ps

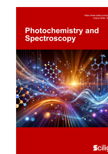

Review

Standing-Wave X-ray Photoemission Spectroscopy (SW-XPS): A Methodological Overview for Non-Destructive Depth Characterization of Buried Interfaces †

Giuseppina Conti [1,*], Henrique Perin Martins [1] and Slavomir Nemšák [1,2]

1 Advanced Light Source, Lawrence Berkeley National Laboratory, Berkeley, CA 94720, USA
2 Department of Physics and Astronomy, University of California, Davis, CA 95616, USA
* Correspondence: grconti@lbl.gov

† This article is dedicated to Prof. Giuseppe Zerbi in recognition of his outstanding scientific contributions to Spectroscopy. Giuseppina Conti is deeply grateful to Prof. Zerbi for his invaluable guidance and for inspiring a lifelong passion for scientific research.

How To Cite: Conti, G.; Martins, H.P.; Nemšák, S. Standing-Wave X-ray Photoemission Spectroscopy (SW-XPS): A Methodological Overview for Non-Destructive Depth Characterization of Buried Interfaces. *Photochemistry and Spectroscopy* **2026**, *2*(2), 9. https://doi.org/10.53941/ps.2026.100020

Received: 21 November 2025
Revised: 6 April 2026
Accepted: 8 April 2026
Published: 3 June 2026

Abstract: Buried interfaces govern the functional properties of a wide range of technologically important material systems, from complex oxide heterostructures and spintronic multilayers to photoresist films and electrochemical interfaces. Yet their non-destructive, chemically specific, and depth-resolved characterization remains one of the central analytical challenges in modern materials science. This paper reviews the methodology of standing-wave X-ray photoelectron spectroscopy (SW-XPS), a synchrotron-based technique that combines the chemical and electronic state sensitivity of XPS with intrinsic depth selectivity, providing non-destructive access to buried interfaces with nanometer to sub-nanometer depth resolution across a multilayer stack. Two principal geometries are reviewed: Bragg-reflection SW-XPS, suited to periodic multilayer systems, and near-total-reflection SW-XPS (NTR-XPS), applicable to any smooth reflective substrate. Although originally developed for solid/solid interface characterization, SW-XPS has recently been extended to solid/gas and solid/liquid interfaces. Through two illustrative case studies drawn from the authors' previously published work, Bragg-reflection SW-XPS applied to a multiferroic heterostructure, and NTR-XPS applied to EUV lithography photoresist films, the analytical capabilities of each geometry are demonstrated. This overview is aimed at spectroscopists new to the technique and at researchers seeking a non-destructive, depth-resolved alternative to established interface characterization methods.

Keywords: X-ray photoemission; standing wave X-ray photoemission; near-total reflection X-ray photoemission; solid/solid interfaces

1. Introduction

1.1. The Centrality of Interfaces in Modern Materials

The critical role of interfaces in determining the properties and performance of modern materials and devices was highlighted by Herbert Kroemer, Nobel Laureate in Physics (2000), who declared in his Nobel Prize lecture: "*The interface is the device*" [1]. Although originally directed at semiconductor thin films for photonic and electronic applications, this insight has since inspired interdisciplinary research across materials science, surface chemistry, and device engineering.

Copyright: © 2026 by the authors. This is an open access article under the terms and conditions of the Creative Commons Attribution (CC BY) license (https://creativecommons.org/licenses/by/4.0/).
Publisher's Note: Scilight stays neutral with regard to jurisdictional claims in published maps and institutional affiliations.

As functional materials grow increasingly complex, with architectures built around carefully engineered heterostructures (buried interfaces and nanoscale multilayers), the demand for analytical techniques capable of probing these interfaces non-destructively, with both chemical and electronic specificity, has grown considerably. Complex oxide heterostructures exhibit remarkable emergent phenomena at their engineered interfaces, absent in their constituent bulk materials, such as two-dimensional electron gases, high-temperature superconductivity, ferroelectricity, and anomalous transport, while electrode–electrolyte interfaces govern the performance of energy storage and conversion devices. Synchrotron-based investigations of such buried solid/solid interfaces, as well as electrode–electrolyte interfaces relevant to energy storage, are well-documented in the literature [2–4].

Beyond solid/solid systems, interfaces between solids and gases or liquids are central to catalytic processes, energy conversion, environmental remediation, and electrochemical charge transfer. Despite their broad scientific and technological importance, only a limited number of studies have addressed solid/gas and solid/liquid interfaces owing to significant experimental challenges [5,6]. The *in situ* and *in operando* characterization of these interfaces requires state-of-the-art techniques to correlate structure and properties with system performance. A major advance in studying such interfaces came with the development of Ambient Pressure X-ray Photoelectron Spectroscopy (APXPS) [7–9]. Spectroscopic techniques for solid/liquid interfaces are extensively reviewed by F. Zaera [10]. This asymmetry between scientific importance and analytical accessibility makes the development of versatile, non-destructive depth-profiling techniques a high priority.

1.2. Limitations of Existing Analytical Techniques

No single established technique fully meets the demand for simultaneous non-destructive access, chemical and electronic specificity, and nanometer-scale depth resolution at buried interfaces. Existing methods are constrained by one of three limitations: destructive character, insufficient depth selectivity, or the absence of chemical and electronic state information.

1.2.1. Destructive methods:

Secondary ion mass spectrometry (SIMS) and ion-sputtering Auger electron spectroscopy (AES) offer excellent elemental sensitivity but introduce artifacts through progressive material removal, atomic mixing, and chemical state modification [11–13]. Transmission electron microscopy (TEM/STEM-EELS) [14] and energy-dispersive X-ray spectroscopy (EDS) [15], deliver atomic-resolution structural and compositional images but require destructive focused-ion-beam sample preparation and yield only localized information.

1.2.2. Non-destructive structural methods:

X-ray reflectometry (XRR) and neutron reflectometry (NR) provide sub-nanometer precision in layer thickness and interface roughness but yield no direct chemical or electronic state information [16].

Standard XPS and angle-resolved XPS (ARXPS) provide the chemical specificity that reflectometry lacks, but are confined to the outermost few nanometers. Hard X-ray photoelectron spectroscopy (HAXPES) extends the probing depth to 10–30 nm without intrinsic depth selectivity, so all layers within the probing volume contribute simultaneously to the signal [17–21].

Vibrational spectroscopy techniques (FT-IR, Raman, ATR-FTIR, nano-FT-IR, TERS) offer non-destructive molecular fingerprinting but are surface-confined and lack access to core-level binding energies, oxidation states, or depth-resolved electronic structure. They are best regarded as powerful complements to XPS-based methods in a multimodal analytical strategy [22–24].

SW-XPS uniquely overcomes all three limitations simultaneously: it is non-destructive, chemically and electronically specific, and provides intrinsic depth selectivity with nanometer to sub-nanometer resolution across the full multilayer thickness, capabilities that no single competing technique can match.

1.3. Standing-Wave XPS: Bridging the Analytical Gap

Standing-wave XPS (SW-XPS) addresses these limitations by integrating the chemical and electronic state sensitivity of XPS with the intrinsic depth selectivity of a standing X-ray wave generated within the multilayer stack itself. By scanning the photon energy or incidence angle across a Bragg reflection condition, the nodes and antinodes of the standing wave sweep through the sample with sub-nanometer precision, selectively enhancing the photoemission signal from specific depths. This yields non-destructive, chemically specific, and depth-resolved information across the full multilayer thickness, including deeply buried interfaces inaccessible to all other surface-sensitive techniques. Recent methodological advances have extended SW-XPS to solid/gas and solid/liquid

systems, considerably broadening its analytical scope. Through representative studies of solid/solid interface depth profiling and chemical characterization, we illustrate the capabilities of this integrated approach and demonstrate how it yields structural and compositional insights at buried interfaces inaccessible to conventional analytical methods.

This paper presents a methodological overview of SW-XPS aimed at spectroscopists new to this technique [19,25–27].

SW-XPS has been applied across a range of research groups and material systems. Foundational contributions by Batterman [28], Bedzyk [29], and Fadley [30,31] established the theoretical and experimental framework of the technique. Zegenhagen et al. [32] developed SW-XPS extensively for surface structure determination at single-crystal interfaces. Woicik and coworkers [33] applied hard X-ray SW-XPS to semiconductor and oxide thin films. More recently, Nemšák, Fadley, and Bluhm demonstrated SW-XPS under ambient-pressure conditions for solid/gas and solid/liquid interfaces [34], while Abruña [5] and Karslıoğlu [35] pioneered its application to electrochemical systems. The application of SW-XPS to solid/gas and solid/liquid systems is not addressed here, comprehensive treatments of these contributions are available in the review literature already cited [34,35].

1.4. Paper Organization

Section 2 describes the principles of SW-XPS, covering the Bragg and NTR geometries, a comparison of their characteristics and a discussion of practical limitations.

Section 3 presents one illustrative case study: Bragg-reflection SW-XPS applied to a BFO/LSMO multiferroic heterostructure, (Bragg geometry).

Section 4 presents a second illustrative case study: NTR-XPS applied to EUV photoresist films, (NTR geometry).

Section 5 provides conclusions.

2. Principles of Standing-Wave X-ray Photoelectron Spectroscopy (SW-XPS)

2.1. Basic Principles

X-ray photoelectron spectroscopy (XPS) is a surface-sensitive analytical technique based on the photoelectric effect: when a material is irradiated with X-rays of sufficient energy, core electrons are ejected from atoms near the surface, and their measured kinetic energies uniquely identify the elements present as well as their chemical bonding states. Because emitted photoelectrons lose energy through inelastic collisions as they travel through the solid, only those generated within the topmost few to tens of nanometers can escape and be detected [17,18]. This finite inelastic mean free path (IMFP) [36] both defines and limits the probing depth of XPS.

The accessible probing depth scales with the excitation energy: soft X-rays (below ~2 keV) sample only the outermost few nanometers, whereas tender (2–5 keV) and hard X-rays (above 5 keV) extend the escape depth to several tens of nanometers. Even so, in a conventional XPS experiment all layers within the probing volume contribute simultaneously to the detected signal, and there is no inherent mechanism to isolate the response of a specific buried layer or interface.

SW-XPS overcomes this limitation by exploiting X-ray interference. When a coherent X-ray beam is reflected from a suitable medium, a single crystal, an engineered multilayer mirror, or a smooth planar surface, it interferes with the incident beam to produce a spatially periodic modulation of the electromagnetic field intensity: an X-ray standing wave. The nodes (intensity minima) and antinodes (intensity maxima) of this standing wave are fixed in space relative to the reflecting planes, but can be swept continuously through the sample by varying the angle of incidence or the photon energy. Because the photoelectron yield from any given depth is proportional to the local X-ray field intensity at that depth, sweeping the standing wave through the sample selectively enhances or suppresses the signal from successive layers. Recording XPS intensities as a function of angle or energy encodes depth-resolved chemical and electronic information non-destructively [19,25,26,37].

Two principal geometries are employed to generate the standing wave, each suited to different sample architectures and depth ranges. Bragg-reflection SW-XPS exploits first-order reflection from a periodic layered structure, a superlattice, a synthetic multilayer mirror, or single crystal, and provides a standing wave period matched to the bilayer repeat, typically in the 2–10 nm range. Near-total-reflection SW-XPS (NTR-XPS) uses grazing-incidence reflection from any sufficiently smooth planar surface near the critical angle, generating a standing wave with a much longer period (tens of nanometers) without requiring a specialized periodic substrate. Both approaches are described in detail below [38].

2.2. Standing Wave Generated at the Bragg Reflection

The X-ray standing wave method in the Bragg geometry was first described and experimentally demonstrated by Batterman more than fifty years ago using a laboratory X-ray source [28]. The underlying principle is: a collimated, monochromatic X-ray beam incident on a periodic reflective medium, such as a single crystal, a superlattice, or an engineered multilayer mirror, undergoes constructive interference between the incident and the specularly reflected beams, producing a stationary standing wave whose periodicity matches the lattice plane spacing or bilayer repeat d_{ML} of the reflecting structure [25,26,30,31,38].

For effective standing wave generation, the multilayer or superlattice must consist of alternating layers of materials with appreciably different electron densities (refractive indices), conventionally achieved by pairing high-atomic-number (high-*Z*) and low-*Z* elements. The first-order Bragg reflection condition is:

$$\lambda_x = 2d_{ML}\sin(\theta_{inc.}) \tag{1}$$

where λ is the incident photon wavelength, d_{ML} is the bilayer period of the multilayer, and θ_{inc} is the angle of incidence. The period of the resulting standing wave, λ_{SW}, is:

$$\lambda_{SW}(|E^2|) = \frac{\lambda_x}{2\sin(\theta_{inc.})} = d_{ML} \tag{2}$$

so the standing wave period closely tracks the bilayer spacing. By selecting an appropriate d_{ML}, the experimenter can engineer the standing wave period to match the depth scale of interest, and position the field antinode at any target depth within the stack.

To extract depth-resolved information, the nodes and antinodes must be translated perpendicular to the sample surface. This is accomplished by slightly varying the incidence angle around the Bragg peak ($\theta_{inc} \pm \Delta\theta$), which shifts the phase of the standing wave and sweeps its antinodes through approximately half the bilayer period. As θ_{inc} is scanned across the Bragg condition, the high-intensity antinode moves continuously through the layer stack, successively amplifying photoemission from each depth (Figure 1). Two alternative approaches, slightly scanning the photon energy at fixed angle, or growing the sample on a wedged substrate, provide equivalent displacements but are experimentally more demanding and rarely employed in practice.

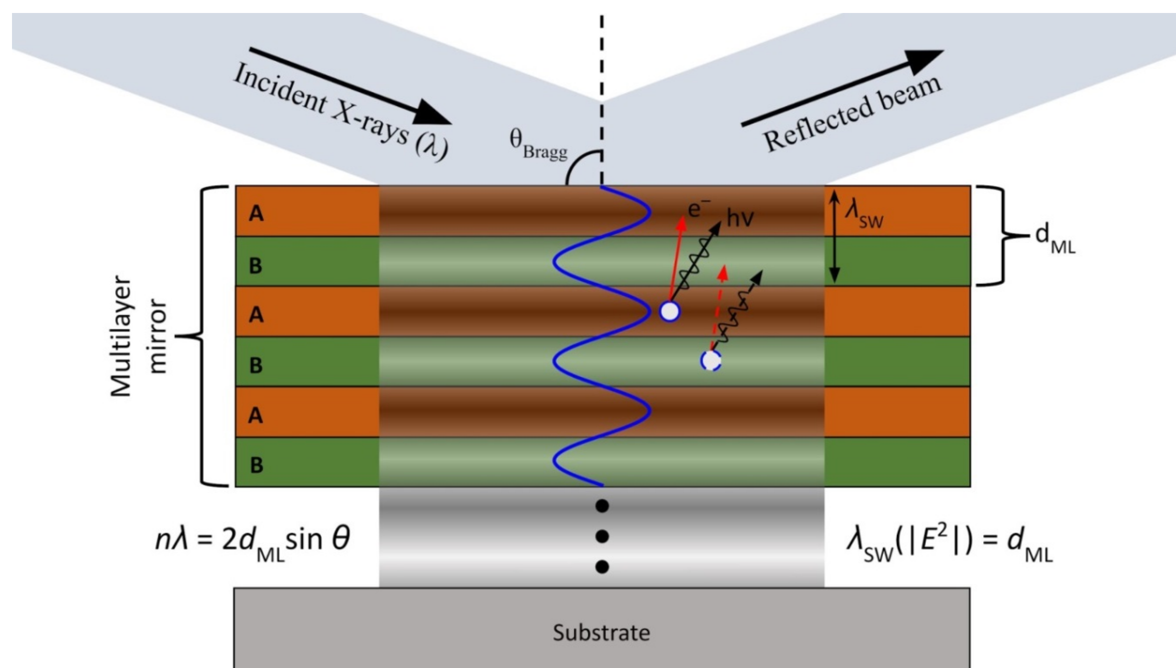

Figure 1. Schematic illustration of standing wave formation from a multilayer mirror in first-order Bragg reflection, showing translation of the antinode through the layer stack as the incidence angle is varied around the Bragg peak. (Reprinted/adapted with permission from Conti et al., J. Micro/Nanopatterning Mater. Metrol. 2021, 20, 034603. [39]).

The modulation amplitude of the standing wave intensity depends on the reflectivity *R* of the mirror: the intensity varies between $1 + R \pm 2\sqrt{R}$. Notably, even modest reflectivity is sufficient for practical SW-XPS experiments: a multilayer with approximately 1% peak reflectivity still yields an intensity modulation of roughly ±20%, which is experimentally resolvable. This relaxed reflectivity requirement considerably broadens the range

of usable multilayer systems, although the overall structural quality of the mirror remains critical for generating a well-defined standing wave.

The primary experimental observable in Bragg SW-XPS is the photoemission rocking curve (RC): the XPS core-level intensity of a chosen element recorded as a function of the incidence angle across the Bragg reflection. Because chemically identical atoms located at different depths experience different local field intensities as the standing wave sweeps through, their contributions to the total signal modulate with different phases and amplitudes. This depth-dependent modulation produces characteristic RC lineshapes that can differentiate and locate emitters at distinct depths, even when they are chemically identical.

Quantitative depth profiling requires comparison of the experimental RCs with simulated profiles. The Yang X-ray Optics (YXRO) code [40], developed in Fadley's group, provides the principal computational framework for this purpose, combining X-ray optical calculations (incorporating absorption, reflection, and the standing wave field profile) with photoemission parameters (photoionization cross-sections and electron attenuation lengths). Structural models, specifying layer thicknesses, compositions, and interfacial roughness, are iteratively refined until the calculated RCs achieve optimal agreement with experiment, yielding quantitative, depth-resolved chemical concentration profiles.

A practical consideration in Bragg SW-XPS is that the effective probing depth is ultimately governed by the inelastic mean free path (IMFP) [36] of the photoelectrons which constrains how deep within the stack a signal can be detected regardless of how far the standing wave field penetrates. Accessing interfaces buried more than ~5 nm therefore requires tender or hard X-ray excitation to increase the photoelectron escape depth, making synchrotron radiation with tunable high-energy beamlines the standard experimental platform for this technique.

2.3. Standing Wave Generated at Near-Total Reflection (NTR)

Near-total reflection (NTR) offers an alternative and experimentally simpler route to generating an X-ray standing wave, as it does not require a multilayer mirror or a superlattice as a substrate. At sufficiently small grazing angles, typically between 0.1° and 3° from the sample surface, X-rays impinging on any smooth, dense planar surface undergo nearly complete specular reflection, analogous to total internal reflection phenomena in optics. The critical angle θ_{CR} below which this near-total reflection occurs depends on the electron density of the material and the photon energy, and is typically very small. Interference between the incident and reflected beams in this geometry produces a standing wave field oriented perpendicular to the sample surface.

NTR-XPS was first proposed by Henke in 1972 [41], who demonstrated theoretically and experimentally that near-total reflection substantially enhances the surface sensitivity of XPS for homogeneous semi-infinite samples. Fadley and coworkers subsequently extended the approach to layered systems, using NTR-XPS to determine the thicknesses of carbon overlayers on gold and oxide layers on silicon [42–44]. A key distinction from the Bragg geometry is that NTR requires no specialized substrate: any sufficiently smooth reflective planar surface can serve as the standing wave generator.

The period of the NTR standing wave is given by:

$$D = \frac{\lambda}{2\sin(\theta_{inc.})} \tag{3}$$

where D is the standing wave period and λ is the X-ray wavelength. Because the grazing angles involved are very small, D is correspondingly much larger than λ. In practice, NTR standing waves have periods in the range of tens of nanometers, substantially exceeding the few-nanometer periodicity typical of the Bragg-geometry standing waves making the NTR approach well suited for characterizing thick overlayers, liquid films, and solid/liquid interfaces. A comprehensive description of NTR-XPS is provided in "X-ray Standing Wave Techniques. Encyclopedia of Condensed Matter Physics" [45].

By incrementally increasing θ_{inc} above θ_{CR}, the standing wave period decreases and the first antinode moves progressively closer to the surface, allowing tunable depth sensitivity. Below the critical angle, the X-ray field decays evanescently into the material, rendering the technique highly sensitive to the outermost surface layers. Above the critical angle, the evanescent character diminishes, transmission into the bulk increases, and sensitivity to subsurface and buried interface features is enhanced. The characteristic intensity enhancement at θ_{CR}, known as the Henke peak, arises from constructive interference that maximizes the field intensity at the surface; its angular position can be used to selectively amplify signals from near-surface regions.

The combination of long standing wave periods, grazing incidence geometry, and the absence of any requirement for periodic substrates makes NTR-XPS a versatile complement to Bragg SW-XPS. It is particularly

advantageous for samples deposited on flat, reflective substrates such as polished silicon wafers or gold films, and for *in situ* studies of solid/liquid and solid/gas interfaces where the overlayer may be many tens of nanometers thick.

2.4. Comparison of the Two Geometries

Table 1 summarizes the principal differences between the Bragg and NTR geometries. The Bragg approach provides a standing wave period precisely matched to the bilayer repeat of the multilayer (typically 2–10 nm), offers high depth precision within that period, and is the method of choice for depth profiling of complex multilayer stacks and superlattices with well-defined layer sequences. It requires, however, a periodic reflective substrate and synchrotron radiation with sufficient brightness and monochromaticity to excite a well-defined Bragg reflection. The NTR approach generates a longer-period standing wave (tens of nanometers), requires no periodic substrate, and is applicable to any smooth planar sample surface. It is therefore more broadly accessible and particularly suited to characterizing thick overlayers, surface films, and solid/liquid or solid/gas interfaces. In both cases, experimental rocking curves are compared with calculated profiles, using the YXRO code [40,46] to extract quantitative structural and chemical information with sub-nanometer precision.

Table 1. This table summarizes the principal characteristics of Bragg-reflection and near-total-reflection (NTR) SW-XPS geometries.

Property	Bragg Reflection	Near-Total Reflection (NTR)
Standing wave period	2–10 nm (matched to bilayer repeat)	Tens of nanometers
Substrate requirement	Periodic multilayer, /superlattice/crystal	Any smooth, reflective planar surface
Depth precision	Sub-nm within bilayer period	Lower; suited to thick overlayers
Typical incidence angle	Near Bragg angle (several degrees)	Below critical angle (0.1°–3°)
Radiation source	Synchrotron (tunable, bright)	Collimated laboratory or synchrotron source
Best suited for	Multilayer stacks, superlattices	Thick films, solid/liquid, solid/gas interfaces
Analysis code	YXRO or equivalent	YXRO or equivalent

2.5. Technical Challenges of SW-XPS

Despite its unique analytical capabilities, SW-XPS presents several challenges:

Sample or Substrate requirements: Bragg SW-XPS requires a well-ordered periodic multilayer substrate or a superlattice sample with sufficient reflectivity. NTR-XPS is less restrictive, requiring only a smooth reflective planar surface, but is limited to shallower depth ranges.

Synchrotron dependence: Bragg-reflection SW-XPS requires a tunable, high-brightness synchrotron source, limiting accessibility compared to laboratory-based techniques. NTR-XPS is less demanding in this regard and can in principle be performed with laboratory sources, but better signal-to-noise and inherent collimation of beams favor synchrotron radiation for quantitative depth profiling.

Data analysis complexity: Quantitative interpretation requires iterative fitting with X-ray optical simulations (YXRO/SWOPT) [40,46], which involves model-dependent assumptions regarding layer composition, thickness, and interfacial roughness. The SWOPT optimizer [46] substantially reduces manual effort but does not eliminate the need for careful model construction.

Radiation Damage: For organic and soft-matter samples, photoresists, polymer films, biological interfaces, prolonged synchrotron exposure can induce beam-driven chemistry: bond scission, crosslinking, desorption, and oxidation. Careful dose management, use of attenuating filters, and spectral monitoring for beam-induced changes are essential in such systems, as illustrated in the EUV photoresist case study in Section 4.

Community Adoption and Concentration of Expertise: Perhaps the most significant limitation of SW-XPS as a widely applicable platform, this technique requires a concentration of expertise, from multilayer mirror design and fabrication, to operation of dedicated tender/hard X-ray photoemission beamlines, to the use of specialized standing wave simulation software [26,29,30,40,46].

Despite these challenges, SW-XPS remains a uniquely powerful method for non-destructive interface characterization. By providing an accessible, self-contained description of the SW-XPS methodology, covering physical principles, experimental implementation, data analysis, and representative applications, this paper aims to lower the barrier to entry and encourage broader independent adoption of the technique across the interface science community.

The following sections illustrate the methodology through two case studies: Bragg-reflection SW-XPS (Section 3) and NTR-XPS (Section 4).

3. Standing Wave X-ray Photoemission Generated at the Bragg Reflections: Multiferroic Heterostructures

3.1. Introduction: Materials and Background

A multiferroic is a material that simultaneously exhibits two or more of the following ferroic order parameters: ferromagnetism, ferroelectricity, and/or ferroelasticity. The most technologically significant manifestation of multiferroic behavior is the magneto-electric effect, whereby an applied electric field can control magnetic properties and vice versa [47,48].

Ferroelectric Bismuth Ferrite $BiFeO_3$ (BFO) and ferromagnetic Lanthanum Strontium Manganite $La_{0.7}Sr_{0.3}MnO_3$ (LSMO) are complex perovskite oxide materials that can be integrated as thin-film heterostructures, in which their intrinsic order parameters, ferroelectricity in BFO and ferromagnetism in LSMO, become intimately coupled at the interface [49,50]. These interactions give rise to a variety of novel magnetic effects, including interface-induced magnetization in the BFO layer and modifications to the magnetic behavior of LSMO driven by epitaxial strain, electronic charge transfer, and lattice coupling. BFO/LSMO heterostructures therefore represent an archetypal hybrid multiferroic system in which BFO's ferroelectric behavior coexists with LSMO's ferromagnetism within a single integrated structure. The quality of the interface plays a decisive role: even subtle variations in atomic intermixing and interdiffusion create distinct nanoscale chemical and electronic environments that govern the emergent functional properties. These heterostructures are regarded as promising candidates for advanced non-volatile memory devices, magnetic sensors, and next-generation spintronic applications.

BFO is the most prominent room-temperature multiferroic material, exhibiting both ferroelectric and antiferromagnetic order [51], with a ferroelectric Curie temperature of T_C = 1100 K and a Néel temperature of T_N = 640 K. However, the electrical and magnetic performance of BFO is significantly compromised by Bi^{3+} volatility during synthesis and by associated oxygen vacancy formation, which induces Fe valence fluctuations ($Fe^{3+} \rightarrow Fe^{2+}$), increased leakage currents, and degraded ferroelectric switching.

LSMO, by contrast, is a doped manganite perovskite exhibiting near-half-metallic ferromagnetism [52,53] with a Curie temperature of $T_C \approx 370$ K and colossal negative magnetoresistance (CMR) [54]. Its magnetic and electronic transport properties are highly sensitive to film thickness, epitaxial strain, growth technique, and deposition conditions, making precise control of the LSMO layer essential for achieving predictable heterostructure behavior [55,56].

Although BFO/LSMO heterostructures have been extensively studied using conventional spectroscopic techniques and first-principles theoretical approaches [57], obtaining depth-resolved experimental information remains a significant challenge. A fundamental open question concerns whether novel electronic or magnetic states emerge at the atomic-scale BFO/LSMO interface, and what physical mechanisms underlie these emergent properties. Interfacial interdiffusion plays a critical role in this regard, as interface morphology, ranging from atomically abrupt to progressively intermixed, dramatically affects the resulting magnetic behavior. Given BFO's inherent chemical instabilities and LSMO's highly anisotropic properties, advanced depth-sensitive characterization techniques such as SW-XPS are essential for accurately determining the depth-resolved electronic structure at the surface, bulk, and buried interfaces of these systems. In the follow section, we report the work previously published by Rault [58] and Martins [59] presenting a detailed SW-XPS characterization of BFO/LSMO superlattices, combining Bragg-reflection and near-total-reflection geometries to achieve sub-unit-cell depth resolution.

3.2. Experimental

All experimental data were acquired at the NIMS Contract Beamline BL15XU, SPring-8 synchrotron facility, Hyogo, Japan [60,61]. Spectra were collected at a photon energy of hν = 5953.4 eV with a total energy resolution of approximately 240 meV, provided by a Si(111) double-crystal monochromator in combination with a Si(333) channel-cut post-monochromator. At this photon energy, the inelastic mean free path (IMFP), estimated using the TPP-2M predictive formula of Tanuma, Powell, and Penn [36], yields an electron information depth of 50–70 Å, corresponding to approximately the first three bilayers of the superlattice and encompassing ~95% of the total photoemission signal. Rocking curves were acquired by scanning the incidence angle θ from 0° to 1.84° in steps of 0.01°, centered on the first-order Bragg angle $\theta_B = 1.35°$.

3.3. Data Acquisition and Analysis

Figure 2 shows a schematic of the BFO/LSMO superlattice consisting of ten bilayer repetitions of 6 unit cells (u.c.) of BFO deposited on 6 u.c. of LSMO for ten repetitions ($[BFO_{6u.c.}/LSMO_{6u.c.}]_{\times 10}$), with the experimental parameters. Depth-resolved XPS measurements are obtained by scanning the incidence angle θ_{inc} across the first-order Bragg reflection, where the period of the standing wave electric field matches the superlattice periodicity d_{ML}. As the incident angle θ_{inc} is scanned, the standing wave field undergoes a phase shift that translates the antinode positions vertically through the sample by one-half period across the full angular range. This selective redistribution of the electric field intensity enhances or suppresses the photoemission yield from specific depths as a function of angle. The core-level and valence-band spectra acquired at each θ_{inc} are integrated and plotted as a function of θ_{inc} to generate photoemission rocking curves (RCs). The phase information encoded in these RCs directly reveals the depth distribution of all elements within the probed volume.

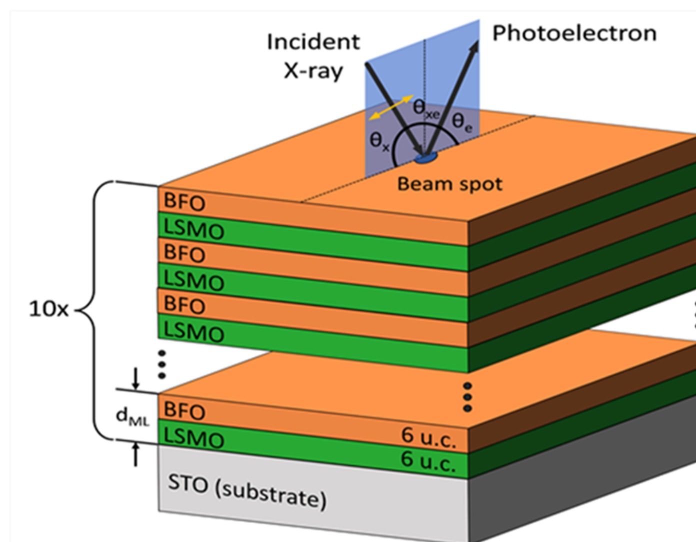

Figure 2. Experimental geometry and the structure of the ($[BFO_{6u.c.}/LSMO_{6u.c.}]_{\times 10}$)-with key parameters defined for a standing-wave study using the multilayer as the standing-wave generator. (Reproduced/modified with permission from Martins et al., arXiv:2012.07993.).

Figure 3a shows representative hard X-ray core-level spectra of the multilayer acquired at an off-Bragg incidence angle: Bi $5d_{5/2}$, O 1s, and Sr $2p_{3/2}$. To extract the rocking curves, the core-level spectrum of each elemental species was fitted at every incidence angle. Shirley background [62,63] subtraction was applied to all datasets, followed by Voigt-lineshape peak fitting using KolXPD software (Kolibrik.net, s.r.o., Czech Republic) [64]. The fitting consistently revealed two spectral components for each core level: a lower binding energy (LBE) peak and a higher binding energy (HBE) peak, attributable to chemically or structurally distinct atomic environments within the heterostructure. Figure 3b displays the RCs of the LBE and HBE components for Bi $5d_{5/2}$, O 1s, and Sr $2p_{3/2}$, obtained by plotting the integrated intensity of each fitted peak as a function of incidence angle. The LBE and HBE components exhibit clearly distinct modulation patterns, confirming that they originate from different depths within the superlattice. To determine the absolute depth distribution of each spectral component, an iterative optimization approach based on X-ray optical and photoemission simulations was employed. A structural model was fitted using the SWOPT black-box optimization program which integrates the Yang X-ray Optics (YXRO) simulation framework with a computationally efficient optimizer to automate the iterative refinement of structural parameters [40,46]. Layer thicknesses and interfacial interdiffusion lengths at each interface were systematically varied to minimize the residual between calculated and experimental RCs for all measured core levels simultaneously.

Figure 4a shows the resulting experimental (dots) and simulated (lines) RCs for the full set of core levels of the ($[BFO_{6u.c.}/LSMO_{6u.c.}]_{\times 10}$) heterostructure: Bi 5d (HBE and LBE), O 1s (HBE and LBE), Fe 2p, Sr 2p (HBE and LBE), La 3d, and Mn 2p. The excellent agreement between experiment and simulation enables precise determination of the chemical structure and composition of the heterostructure. Figure 4b presents the optimized depth-concentration profile of the top three bilayers (probing depth 50–70 Å as determined by the IMFP) [36], including vacuum/BFO surface interface, the bulk BFO and LSMO layers, and the two chemically distinct interface types: BFO-on-LSMO and LSMO-on-BFO. Color gradients at the interfaces represent the interfacial

interdiffusion profiles. Notably, the two interface types exhibit asymmetric interdiffusion behavior, demonstrating the power of SW-XPS to distinguish chemically inequivalent buried interfaces at sub-unit-cell depth resolution.

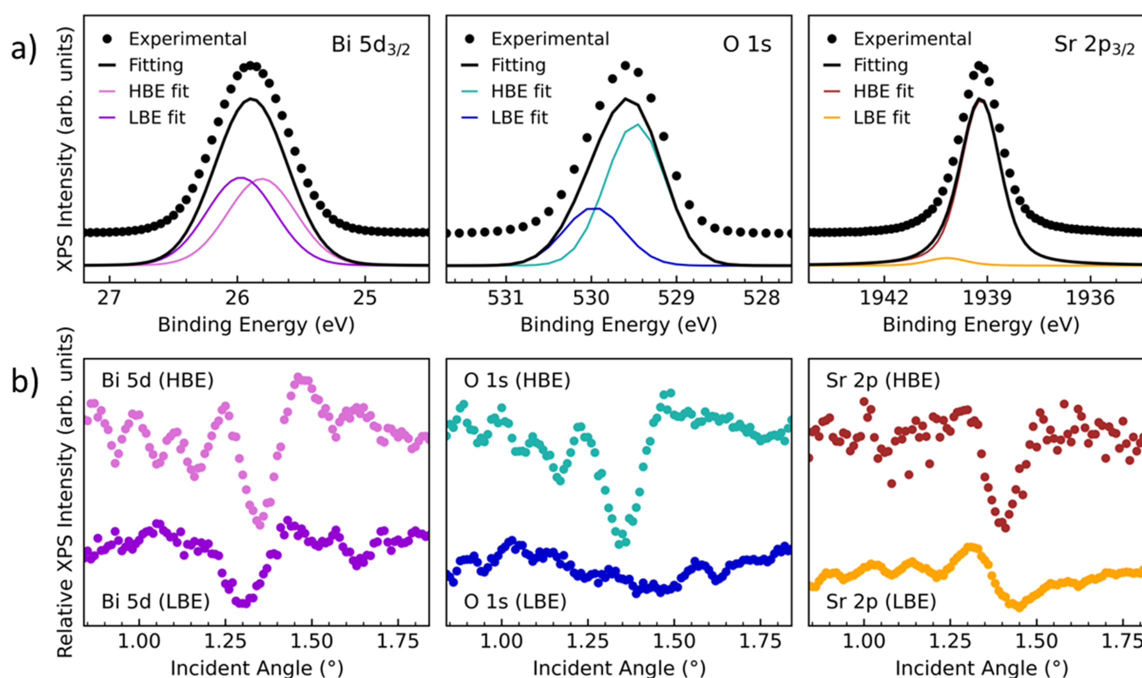

Figure 3. Standing-wave photoemission spectroscopy of the ($[BFO_{6u.c.}/LSMO_{6u.c.}]_{\times 10}$) multilayer measured at hν = 5953.4 eV. (**a**) Representative core-level spectra: Bi $5d_{5/2}$, O 1s, and Sr $2p_{3/2}$ (dots: experimental data). The solid black line is the total curve fit, displaced below the data for clarity; colored lines denote the lower binding energy (LBE) and higher binding energy (HBE) components. (**b**) Photoemission rocking curves of the HBE and LBE components of Bi 5d5/2, O 1s, and Sr 2p3/2 as a function of incidence angle. (Reproduced and modify with permission from Martins et al. [arXiv:2012.07993).

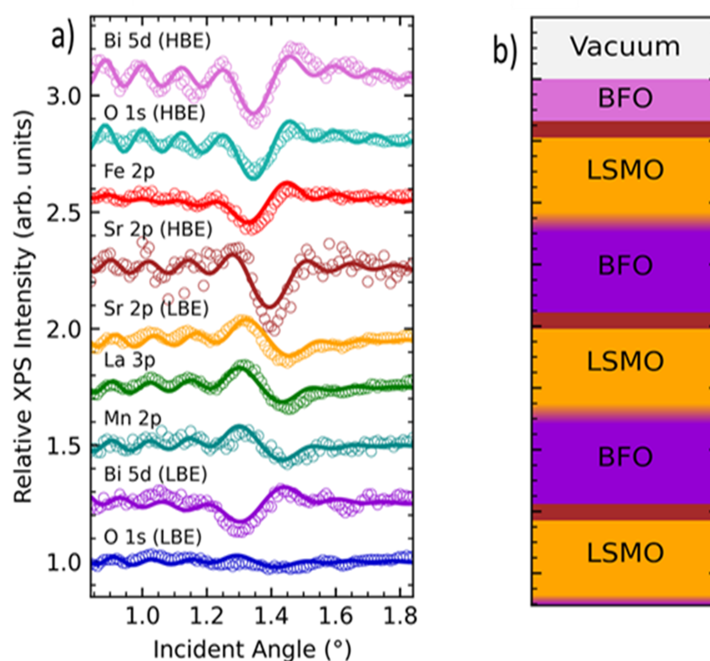

Figure 4. (**a**) Experimental (dots) and simulated (lines) rocking curves for the complete set of measured core levels: Bi 5d (HBE and LBE), O 1s (HBE and LBE), Fe 2p, Sr 2p (HBE and LBE), La 3d, and Mn 2p. (**b**) Optimized depth-concentration profile of the top three BFO/LSMO bilayers, including the vacuum interface, surface BFO layer, BFO/LSMO interface regions, and bulk BFO and LSMO layers. Color gradients represent interfacial interdiffusion profiles. (Reproduced/modified with permission from Martins et al., arXiv:2012.07993).

3.4. Results and Discussion

The optimized depth profiles, as discussed in Martins et al. [59], revealed a pronounced asymmetry between the two interface types within the superlattice.

The BFO-on-LSMO interfaces are atomically sharp, within the resolution limit of the SW method, whereas the LSMO-on-BFO interfaces exhibit significant interdiffusion extending over approximately 4.8 Å (1.2 u.c.). This asymmetric interdiffusion behavior is consistent with prior neutron reflectometry and magnetometry studies of analogous BFO/LSMO superlattice systems [65]. Furthermore, the sharp BFO-on-LSMO interfaces were found to be Sr-enriched. These interfacial Sr species were attributed to the higher binding energy (HBE) component observed in the Sr 2p core-level spectra, and are spatially confined within approximately 4.2 Å (~1 u.c.) of the interface. This localized Sr accumulation likely modifies the local electrostatic potential and orbital hybridization, thereby influencing the electronic coupling between the BFO and LSMO layers.

The depth distribution of Bi species also provides important chemically information. The Bi 5d core-level spectrum of the top $BiFeO_3$ layer is dominated exclusively by a HBE component attributed to surface oxidation occurring during air exposure prior to measurement. In contrast, Bi 5d core -level of the Bi atoms in all buried BFO layers contribute exclusively to the lower binding energy (LBE) component, consistent with Bi in the standard $^{3+}$ valence state of bulk $BiFeO_3$.

Building upon the depth-resolved core-level results, the SW-XPS approach was extended to characterize the valence band, providing depth-resolved electronic structure information across the BFO/LSMO interfaces. Distinctive valence band features were resolved for bulk BFO, bulk LSMO, and the interfacial regions, revealing clear depth-dependent variations in the electronic structure. Martins et al. [59] interpreted these observations as direct spectroscopic evidence for emergent interfacial electronic states in the BFO/LSMO system. Complementary first-principles calculations based on the Korringa–Kohn–Rostoker (KKR) Green's function method could provide further insight into the origin and character of these interfacial electronic states [66,67].

3.5. Summary

Martins et al. [59], demonstrated layer-resolved chemical and electronic characterization of the BFO/LSMO hybrid multiferroic heterostructure, establishing a clear methodological benchmark for the field. SW-XPS uniquely combines non-destructive depth profiling with simultaneous sensitivity to both compositional and electronic-structure information at buried complex-oxide heterointerfaces, capabilities that are uniquely difficult to replicate with other techniques at this level of depth resolution. Without requiring cross-sectional sample preparation, it provides artifact-free access to interfacial properties in the as-grown state. These attributes make SW-XPS a particularly powerful and versatile tool for the characterization of functional oxide interfaces across a broad range of complex oxide heterostructures.

4. SW-XPS Generated at Near-Total Reflection (NTR-XPS): EUV Photoresist Characterization

4.1. Introduction: Background and Materials

As semiconductor manufacturers actively optimize photoresist formulations and processing conditions to meet the requirements of industrial-scale fabrication, accurate characterization of the physical and chemical properties of resist films at each processing stage remains a critical challenge [68,69]. To demonstrate the analytical capabilities of NTR-XPS, this section presents a study of an organic photoresist designed for extreme ultraviolet (EUV) lithography, previously reported in literature by Martins et al [39,70].

Chemically amplified resists (CARs) constitute the prevalent class of EUV photoresists [71,72]. A typical CAR formulation contains three key constituents: a polymer resin matrix; a photoacid generator (PAG) that confers sensitivity to ultraviolet radiation; and a dissolution inhibitor that governs resist solubility before and after exposure. Following spin-coating onto a substrate, CARs are processed through four sequential stages: (1) post-application bake (PAB) which removes residual solvent and moisture from the film; (2) patterned EUV exposure; (3) post-exposure bake (PEB); (4) wet chemical development.

During EUV exposure, selected regions of the photoresist film are irradiated with photons at a wavelength of 13.5 nm. Absorption of these photons generates high-energy photoelectrons that undergo elastic and inelastic scattering throughout the resist matrix, transferring energy to neighboring molecules. In CARs, these energy-transfer processes drive polymer chain scission and/or crosslinking reactions. NTR-XPS is particularly well-suited for identifying and characterizing this radiation-induced chemical damage.

4.2. Experimental

Commercial CAR films were spin-coated onto Si-terminated $[Mo/Si]_{60}$ multilayer mirror substrates to an initial thickness of approximately 14 nm and subsequently subjected to a post-application bake (PAB) following standard EUV photoresist fabrication procedures, which reduced the resist thickness to approximately 10 nm. Although NTR characterization requires only a smooth, reflective substrate, a $[Mo/Si]_{60}$ synthetic superlattice mirror, consisting of 60 alternating Mo and Si layers with a nominal periodicity of 10 nm, was used to enable complementary Bragg-reflection SW-XPS analysis on the same sample [39,70].

Photoemission experiments were performed at the Advanced Light Source (ALS), Lawrence Berkeley National Laboratory, Berkeley, California, using incident photons at 3 keV with an energy resolution better than 500 meV. Experimental data were analyzed and fit using the YXRO package for X-ray optical and photoemission simulations [40]. Depth-profile optimization was carried out using SWOPT (Standing Wave Optimizer), a global optimization algorithm integrating a surrogate model with a black-box optimizer [46].

Schematic illustrations of the CAR processing steps and the sample's layered architecture are shown in Figure 5a,b, respectively.

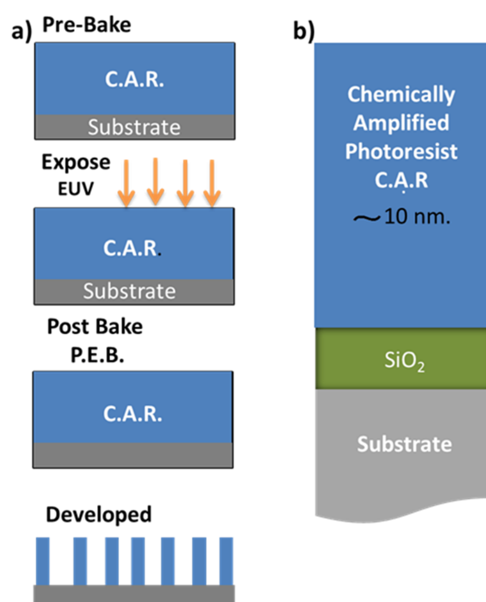

Figure 5. (**a**) Schematic of the standard processing protocols of EUV exposure steps of the chemically amplified photoresist (CAR); (**b**) Sample schematics deposited on a Si substrate. (Reproduced/modified with permission from Martins et al., *J. Phys. D Appl. Phys.* 2021, *54*, 464002).

The post-application bake induced a thickness reduction of the photoresist from approximately 14 nm to 10 nm.

The NTR-XPS experiment reported in ref. [70] was designed to characterize the structural and chemical properties of the CAR films in this post-baked state.

4.3. Data Acquisition and Analysis

The NTR experiment involves acquiring core-level spectra at systematically incremented incidence angles, spanning from 0° (grazing incidence) to a few tenths of a degree beyond the critical angle (θ_c). Figure 6a shows hard X-ray photoelectron spectra and their corresponding fits for the S 1s, C 1s, and F 1s core levels of the CAR film and the Si 1s core level of the underlying substrate. A Shirley background was subtracted from all spectra before fitting, and pseudo-Voigt functions were used to fit each peak component [62–64].

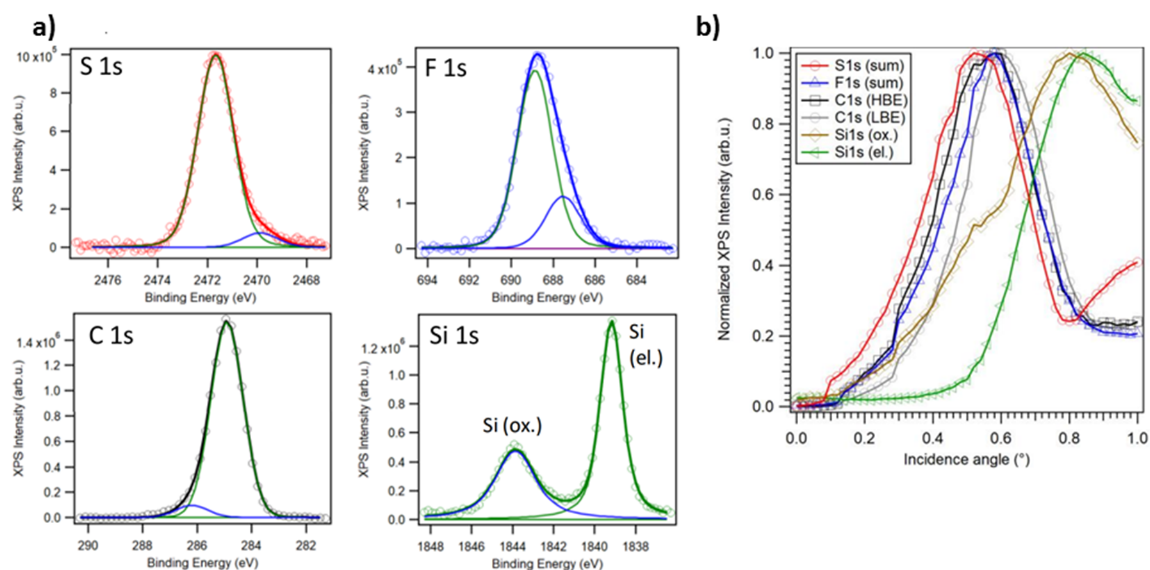

Figure 6. (**a**) XPS core levels spectra of the CAR film after PAB: S 1s, F 1s, C 1s; and Si 1s from the substrate. (**b**) NTR rocking curves, experimental (solid lines) and simulated (dots) (Reproduced/modified with permission from Martins et al., *J. Phys. D Appl. Phys.* 2021, *54*, 464002).

Both the S 1s and F 1s core levels exhibit two well-resolved peaks, corresponding to distinct chemical environments. The C 1s spectrum is similarly decomposed into two components: a lower binding energy (LBE) contribution attributed to C–C and C–H functional groups, and a higher binding energy (HBE) contribution associated with C=O, C–O, and C–F functional groups. The Si 1s spectrum displays two well-separated peaks, corresponding to elemental Si^0 from the silicon substrate and Si^{4+} from the native oxide overlayer. The integrated intensities of these core-level peaks are plotted as a function of incidence angle in Figure 6b, yielding element- and species-specific rocking curves.

The NTR rocking curves (RCs) in Figure 6b show experimental data as solid lines and simulated curves as dots. The sequence of low-angle intensity onsets and peak maxima directly encodes the elemental depth profile, confirming the layered sample architecture from surface to substrate. Starting from the surface, the S 1s signal (red) appears first, followed by the HBE C 1s (black) and F 1s (blue) contributions at intermediate angles, and then the LBE C 1s (gray) near 0.55°. The Si 1s signal from the native oxide (light brown) emerges at 0.80°, followed by that from the Si^0 substrate (green) at 0.84°. The simulated RCs closely reproduce the experimental progression, validating the assigned layer ordering from surface to substrate.

These rocking curves were compared with simulated profiles calculated using the YXRO [40] and SWOPT [46] codes, following the iterative optimization procedure described in Section 3.3.

4.4. Results and Discussion

Figure 7 reports the depth profiles showing the distribution of each layer as determined by fitting the experimental RCs to optimized model parameters, revealing clear chemical stratification within the film: HBE carbon species (C=O, C–O, C–F) are concentrated in the upper portion of the photoresist, while LBE carbon species (C–C, C–H) extend throughout the entire resist layer to the silicon oxide interface.

Accurate reproduction of the Si^{4+} peak required the inclusion of a sub-monolayer SiO_x contamination layer at the photoresist surface, most likely attributable to adventitious contamination introduced during substrate dicing.

Two independent fits were performed using the HBE and LBE carbon distributions separately, together with the SiO_x layers. The HBE and LBE carbon fits yielded total photoresist thicknesses of 9.4 nm and 10.7 nm, respectively, both in excellent agreement with the nominal ~10 nm thickness after PAB.

The fitting further identified a ~2.8 nm surface layer composed exclusively of HBE carbon species (C=O, C–O, C–F), and a ~2.8 nm interfacial region at the substrate boundary enriched in LBE carbon species (C–C, C–H). These chemical gradients at the top and bottom interfaces were attributed to two distinct mechanisms. At the air-exposed top surface, thermal treatment during PAB likely induces partial degradation of the polymer C–C backbone, depleting LBE carbon species in the uppermost region. At the substrate interface, radiation chemistry is expected to dominate: low-energy secondary electrons generated from the substrate during X-ray illumination

modify the resist chemistry through bond scission and oxidation reactions, producing an interfacial region enriched in LBE carbon at the expense of C=O, C–O, and C–F species.

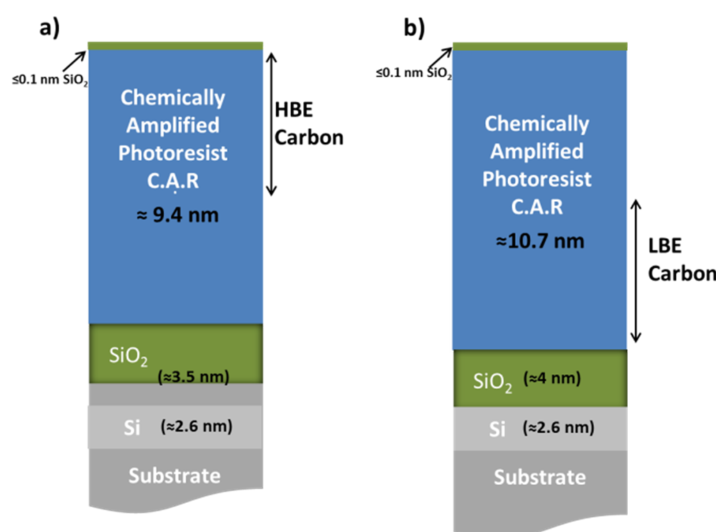

Figure 7. Depth profiles showing the distribution of each layer as determined by fitting the experimental RCs to optimized model parameters: (**a**) HBE carbon species; (**b**) LBE carbon species. (Reproduced/modified with permission from Martins et al., *J. Phys. D Appl. Phys.* 2021, *54*, 464002).

Independent Bragg-reflection SW-XPS analysis [39,70] indicated a total photoresist film thickness of approximately 9 nm; the ~1 nm discrepancy relative to the NTR result falls within experimental uncertainty.

The two techniques are mutually reinforcing: NTR-XPS provides exceptional sensitivity for chemical depth profiling, while Bragg-reflection SW-XPS excels at detecting buried interfaces and trace contaminants. Together, they deliver a level of structural and chemical characterization that neither method can achieve independently

4.5. Summary

Near-total reflection X-ray combined with photoelectron spectroscopy (NTR-XPS) showed approximately 1nm depth resolution at a EUV lithography photoresist/Si–SiO_2 interface. NTR-XPS resolved two distinct carbon chemical states: HBE carbon species (C=O, C–F, and C–O) concentrated at the film surface and depleted near the substrate and LBE carbon species (C–C, C–H) dominating the bulk and depleted at the surface. Layer thicknesses determined from independent HBE and LBE carbon fits were mutually consistent and in excellent agreement with the nominal post-PAB resist thickness.

This methodology is broadly applicable to layered or chemically graded material systems and buried interfaces. Importantly, it delivers standing-wave spectroscopy capabilities without requiring an artificial multilayer mirror, making it uniquely powerful for *in situ and in operando* studies of solid/gas and solid/liquid interfaces. These capabilities complement those of the Bragg-reflection geometry demonstrated in Section 3, and together establish SW-XPS as a robust and comprehensive platform for non-destructive, chemically specific, depth-resolved characterization of functional material interfaces.

5. Conclusions

SW-XPS has matured into a uniquely capable platform for the non-destructive, chemically specific, depth-resolved characterization of buried interfaces, a combination of properties that no single competing technique achieves. The two geometries reviewed here are complementary by design: Bragg-reflection SW-XPS delivers sub-unit-cell depth precision within a periodic multilayer, making it the method of choice for complex oxide heterostructures and spintronic systems where emergent interfacial phenomena are governed by atomic-scale chemistry; NTR-XPS, requiring no periodic substrate, extends these capabilities to organic films, solid/liquid, and solid/gas interfaces accessible under realistic *in situ* and *in operando* conditions.

The principal barrier to wider adoption is not scientific but practical: the technique demands synchrotron access, specialized multilayer samples, and expertise in X-ray optical simulation. This is the primary motivation for the present overview.

The ongoing development of dedicated multimodal endstations, notably the Ambient Pressure Photo-Emission and X-ray Scattering (APPEXS) endstation at beamline 11.0.2 of the Advanced Light Source (Lawrence Berkeley National Laboratory) [73], simultaneously combines ambient-pressure XPS (AP-XPS) with grazing-incidence X-ray scattering (GIXS) under realistic reaction conditions. The planned integration of Raman spectroscopy and FT-IR into this endstation suggests a transition from a specialist tool to a more broadly accessible multimodal platform, capable of simultaneously delivering chemical, structural, and vibrational information with nanometer depth resolution under operationally realistic conditions, capabilities essential for advancing heterogeneous catalysis, sustainable energy, and next-generation microelectronics. The open availability of simulation codes such as YXRO [40] and SWOPT [46] is similarly lowering the barriers to entry. The interface science community stands to benefit substantially from this wider adoption. Wherever the functional properties of a material system are determined at a buried interface, in oxide electronics, spintronics, energy storage, catalysis, or advanced lithography, SW-XPS offers a path to quantitative, depth-resolved, chemically specific answers that are simply not available by other means.

Author Contributions

G.C. participated at the experimental work for both BFO/LSMO and EUV photoresists collecting the data and analyzing them. She wrote the manuscript. H.P.M. analyzed the data from the BFO/LSMO standing-wave experiment and contributed to this manuscript. He also participated in collecting and analyzing the EUV photoresists data. S.N. conceptualized the projects, led the NTR-XPS data collection and all data analysis, and edited the manuscript. All authors have read and agreed to the published version of the manuscript.

Funding

The authors declare that this methodological overview was produced without dedicated funding. Financial support for the individual research studies referenced herein is reported in the corresponding original publications.

Institutional Review Board Statement

Not applicable.

Informed Consent Statement

Not applicable.

Data Availability Statement

We advocate for the sharing of research data by all authors contributing to publications in Scilight journals. In this section, authors may be asked to provide the raw data of their study together with the manuscript for editorial review and should be prepared to make the data publicly available if practicable. In any event, authors should ensure accessibility of such data to other competent professionals for at least 10 years after publication (preferably via an institutional or subject-based data repository or other data center), provided that the confidentiality of the participants can be protected and legal rights concerning proprietary data do not preclude their release. In instances where novel data were not generated or data remains inaccessible due to privacy or ethical considerations, a clear statement outlining these circumstances is mandatory.

Acknowledgments

We thank all collaborators with whom we shared beam time and discussed results. For the BFO/LSMO project we would like to acknowledge: S. A. Khan, A. A. Greer, A. Y. Saw, G. K. Palsson, M. Huijben, K. Kobayashi, S.Ueda, C. M. Schneider, I. M. Vishik, J. Minár, A. X. Gray. For the EUV Photoresist project we would like to acknowledge: I. Cordova, L. Falling, H. Kersell, F. Salmassi, E. Gullikson, I. Vishik,C. Baeumer, P. Naulleau, C.M. Schneider. We also gratefully acknowledge all co-authors of arXiv:2012.07993 for their agreement to the reuse of the BFO/LSMO data and figures in this methodological overview. Copyright clearance for reproduction of figures from J. Phys. D: Appl. Phys. 54, 464002 (2021) has been obtained from IOP Publishing. Experiments at the Advanced Light Source used Big Blue endstation at the beamline 9.3.1. The Advanced Light Source is a U.S. DOE Office of Science User Facility under contract no. DE-AC02-05CH11231.

Conflicts of Interest

The authors declare no conflict of interest.

Use of AI and AI-Assisted Technologies

The authors used Anthropic as a proofreading aid during manuscript preparation, specifically for identifying typographical and syntax errors. Following this process, the authors reviewed and edited the content as necessary and take full responsibility for the published article.

References

1. Kroemer, H. Quasielectric fields and band offsets: Teaching electrons new tricks. In *Nobel Lecture*; World Scientific Publishing: Singapore, 2002; pp. 449–469.
2. Hwang, H.Y.; Iwasa, Y.; Kawasaki, M.; et al. Emergent Phenomena at Oxide Interfaces. *Nat. Mater.* **2012**, *11*, 103–113.
3. Wandelt, K. *Surface and Interface Science Series*; Wiley-VCH Verlag GmbH & Co. KGaA: Weinheim, Germany, 2020; Volumes 9 and 10; ISBN: 9783527822508.
4. Nemšák, S.; Conti, G.; Gray, A.X.; et al. Energetic, spatial, and momentum character of the electronic structure at a buried interface: The two-dimensional electron gas between two metal oxides. *Phys. Rev. B* **2016**, *93*, 245103.
5. Abruña, H.D.; Bommarito, G.M.; Acevedo, D. The Study of Solid/Liquid Interfaces with X-ray Standing Waves. *Science* **1990**, *250*, 69–74.
6. Conti, G.; Shavorskiy, A.; Bluhm, H.; et al. X-ray standing-wave photoelectron spectroscopy: A powerful method for probing buried interfaces. In *Encyclopedia of Solid-Liquid Interfaces*, 1st ed.; Wandelt, K., Bussetti, G., Eds.; Elsevier: Amsterdam, The Netherlands, 2024; pp. 324–335. https://doi.org/10.1016/B978-0-323-85669-0.00141-0.
7. Salmeron, M.; Schlögl, R. Ambient pressure photoelectron spectroscopy: A new tool for surface science and nanotechnology. *Surf. Sci. Rep.* **2008**, *63*, 169–199.
8. Salmeron, M. From Surfaces to Interfaces: Ambient Pressure XPS and Beyond. *Top. Catal.* **2018**, *61*, 2044–2051. https://doi.org/10.1007/s11244-018-1069-0.
9. Pinder, J.W.; Crossman, J.; Kulbacki, B.; et al. Current trends in near ambient pressure x-ray photoelectron spectroscopy (NAP-XPS). Degree of reporting of instrument parameters. *J. Vac. Sci. Technol.* **2025**, *43*, 063203.
10. Zaera, F. Surface chemistry at the liquid/solid interface. *Surf. Sci.* **2011**, *605*, 1141–1145.
11. Lockyer, N.P.; Aoyagi, S.; Fletcher, J.S.; et al. Secondary ion mass spectrometry. *Nat. Rev. Methods Primers* **2024**, *4*, 32.
12. Hofmann, S.; Zhou, G.; Kovac, J.; et al. Preferential sputtering effects in depth profiling of multilayers with SIMS, XPS and AES. *Appl. Surf. Sci.* **2019**, *483*, 140–155.
13. Hofmann, S. Advances in sputter depth profiling using AES. *Surf. Interface Anal.* **2003**, *35*, 556–563.
14. Song, L.; Mao, R.; Gao, P. Recent progress in electron energy loss spectroscopy with concurrent spatial and momentum resolution. *Microscopy* **2026**, *75*, 76–88. https://doi.org/10.1093/jmicro/dfaf035.
15. Martins, R.C.; Bahia, M.G.A.; Buono, V.T.L. Surface analysis of ProFile instruments by scanning electron microscopy and X-ray energy-dispersive spectroscopy: A preliminary study. *Int. Endod. J.* **2002**, *35*, 848–853.
16. Basu, S.; Singh, S. *Neutron and X-ray Reflectometry: Emerging Phenomena at Heterostructure Interfaces*; IOP Publishing: Bristol, UK, 2022. ISBN: 978-0-7503-4693-1.
17. Stevie, F.A.; Donley, C.L. Introduction to X-ray photoelectron spectroscopy. *J. Vac. Sci. Technol. A* **2020**, *38*, 063204. https://doi.org/10.1116/6.0000412.
18. Fadley, C.S. X-ray photoelectron spectroscopy: Progress and perspectives. *J. Electron. Spectrosc. Relat. Phenom.* **2010**, *178–179*, 2–32.
19. Fadley, C.S. Hard X-ray photoemission with angular resolution and standing-wave excitation. *J. Electron. Spectrosc. Relat. Phenom.* **2013**, *190*, 165–180.
20. Weiland, C.; Rumaiz, A.K.; Pianetta, P.; et al. Recent applications of hard X-ray photoelectron spectroscopy (HAXPES). *J. Vac. Sci. Technol. A* **2016**, *34*, 030801.
21. Feng, C.; Li, Y. Hard X-ray photoelectron spectroscopy for depth-resolved analysis of optoelectronic and photoelectrochemical devices. *J. Phys. Chem. Lett.* **2026**, *17*, 1541–1552.
22. Workman, J., Jr. A review of the latest research applications using FT-IR spectroscopy. *Spectrosc. Suppl.* **2024**, *39*, 22–28.
23. Zerbi, G. *Modern Polymer Spectroscopy*; Wiley-VCH Verlag GmbH: Weinheim, Germany, 1999. ISBN:9783527613922.
24. Nazari, G.; Arami-Niya, A. Raman and tip-enhanced Raman spectroscopy studies of polymer blends: A review. *J. Polym. Res.* **2025**, *32*, 379.
25. Zegenhagen, J. Surface structure determination with X-ray standing waves. *Surf. Sci. Rep.* **1993**, *18*, 199–271.

26. Zegenhagen, J.; Kazimirov, A. X-ray standing waves in a nutshell. In *Applications of the X-ray Standing Wave Technique in Physical Science Research—Synchrotron Light Sources and Free-Electron Lasers*; Springer: Berlin, Germany, 2018; Chapter 1, pp. 1–31.
27. Woicik, J.C. *Hard X-ray Photoelectron Spectroscopy (HAXPES)*; Springer Series in Surface Sciences; Springer: Berlin, Germany, 2016; Volume 59. ISBN: 9783319240411.
28. Batterman, B.W. Effect of Dynamical Diffraction in X-ray Fluorescence Scattering. *Phys. Rev.* **1964**, *133*, A759–A764.
29. Available online: https://bedzyk.mccormick.northwestern.edu/ (accessed on 26 April 2026).
30. Available online: https://fadley.physics.ucdavis.edu/ (accessed on 26 April 2026).
31. Kuo, C.-T.; Conti, G.; Rault, J.E.; et al. Emergent phenomena at oxide interfaces studied with standing-wave photoelectron spectroscopy. *J. Vac. Sci. Technol. A* **2022**, *40*, 020801.
32. Zegenhagen, J.; Kazimirov, A. Series on Synchrotron Radiation Techniques and Applications. In *The X-ray Standing Way Technique. Principles and Applications*; World Scientific Publishing Co.: Singapore, 2013; Volume 7. https://doi.org/10.1142/6666.
33. Woo, H.; Tyson, T.A.; Croft, M.; et al. Correlations between the magnetic and structural properties of Ca-doped $BiMnO_3$. *Phys. Rev. B* **2001**, *63*, 134412.
34. Nemšák, S.; Shavorskiy, A.; Karslıoğlu, O.; et al. Concentration and chemical-state profiles at heterogeneous interfaces with sub-nm accuracy from standing-wave ambient-pressure photoemission. *Nat. Commun.* **2014**, *5*, 5441.
35. Karslıoğlu, O.; Bluhm, H. Ambient-Pressure X-ray Photoelectron Spectroscopy (APXPS). In *Operando Research in Heterogeneous Catalysis*; Springer Series in Chemical Physics; Frenken, J., Groot, I., Eds.; Springer: Berlin, Germany, 2017; Volume 114. https://doi.org/10.1007/978-3-319-44439-0_2.
36. Tanuma, S.; Powell, C.J.; Penn, D.R. Calculations of electron inelastic mean free paths. IX. Data for 41 elemental solids over the 50 eV to 30 keV range. *Surf. Interface Anal.* **2011**, *43*, 689–699.
37. Bedzyk, M.J.; Bommarito, G.M.; Schildkraut, J.S. X-ray standing waves at a reflecting mirror surface. *Phys. Rev. Letters* **1989**, *62*, 1376–1379.
38. Yang, S.-H.; Gray, A.X.; Kaiser, A.M.; et al. Making use of X-ray optical effects in photoelectron-, Auger electron-, and X-ray emission spectroscopies: Total reflection, standing-wave excitation, and resonant effects. *J. Appl. Phys.* **2013**, *113*, 073513.
39. Conti, G.; Martins, H.P.; Cordova, I.A.; et al. Chemical and structural characterization of EUV photoresists as a function of depth by standing-wave x-ray photoelectron spectroscopy. *J. Micro/Nanopatterning Mater. Metrol.* **2021**, *20*, 034603.
40. Available online: https://pyxro.lbl.gov (accessed on 26 April 2026).
41. Henke, B.L. Ultrasoft X-ray reflection, refraction, and production of photoelectrons (100–1000 eV region). *Phys. Rev. A* **1972**, *6*, 94–104.
42. Mehta, M.; Fadley, C.S. X-ray photoelectron spectroscopy using near-total reflection: Theory and application to a gold surface. *Chem. Phys. Lett.* **1977**, *46*, 285–289.
43. Mehta, M.; Fadley, C.S. Angular-dependent X-ray photoemission study of oxidized silicon at low X-ray incidence angles. *Chem. Phys. Lett.* **1977**, *46*, 225–230.
44. Kawa, J.; Hayakawa, S.; Kitajima, Y.; et al. Total reflection X-ray photoelectron spectroscopy. *J. Electron. Spectrosc.* **1995**, *76*, 313–318.
45. Bedzyk, M.J. X-ray standing wave techniques. In *Encyclopedia of Condensed Matter Physics*; Bassani, F., Liedl, G.L., Wyder, P., Eds.; Elsevier: Oxford, UK, 2005; Volume 6, p. 330.
46. Karslıoğlu, O.; Gehlmann, M.; Müller, J.; et al. An efficient algorithm for automatic structure optimization in X-ray standing-wave experiments. *J. Electron. Spectrosc. Relat. Phenom.* **2019**, *230*, 10–20.
47. Eerenstein, W.; Mathur, N.D.; Scott, J.F. Multiferroic and magnetoelectric materials. *Nature* **2006**, *442*, 759–765.
48. Ramesh, R.; Spaldin, N.A. Multiferroics: Progress and prospects in thin films. *Nat. Mater.* **2007**, *6*, 21–29.
49. Yu, P.; Lee, J.-S.; Okamoto, S.; et al. Interface ferromagnetism and orbital reconstruction in $BiFeO_3$–$La_{0.7}Sr_{0.3}MnO_3$ Heterostructures. *Phys. Rev. Lett.* **2010**, *105*, 027201.
50. Wu, S.-M.; Cybart, S.A.; Yu, P.; et al. Reversible electric control of exchange bias in a multiferroic field-effect device. *Nat. Mater.* **2010**, *9*, 756–761.
51. Wang, J.; Neaton, J.B.; Zheng, H.; et al. Epitaxial $BiFeO_3$ multiferroic thin-film heterostructures. *Science* **2003**, *299*, 1719–1722.
52. Banach, G.; Tyer, R.; Temmerman, W.M. Study of half-metallicity in LSMO. *J. Magn. Magn. Mater.* **2004**, *272–276*, 1963–1964.
53. Spaldin, N.A.; Ramesh, R. Advances in magnetoelectric multiferroics. *Nat. Mater.* **2019**, *18*, 203–212.
54. Tokura, Y.; Tomioka, Y. Colossal magnetoresistive manganites. *J. Magn. Magn. Mater.* **1999**, *200*, 1–23.
55. Yang, F.; Kemik, N.; Biegalski, M.D.; et al. Strain engineering to control the magnetic and magnetotransport properties of $La_{0.67}Sr_{0.33}MnO_3$ thin films. *Appl. Phys. Lett.* **2010**, *97*, 092503.

56. Greculeasa, S.G.; Stanciu, A.-E.; Leca, A.; et al. Influence of Thickness on the Magnetic and Magnetotransport Properties of Epitaxial $La_{0.7}Sr_{0.3}MnO_3$ Films Deposited on STO(001). *Nanomaterials* **2021**, *11*, 3389.
57. Tamerd, M.A.; Marjaoui, A.; Zanouni, M.; et al. Electronic, Magnetic, and Ferroelectric Properties of Bi0.9La0.1Fe0.9Mn0.1O3/La0.8Sr0.2MnO3: Experimental and First Principles Calculations Studies. *J. Electron. Mater.* **2024**, *53*, 824–833.
58. Rault, J.E.; Kuo, C.-T.; Martins, H.P.; et al. High resolution depth profiling using near-total-reflection hard x-ray photoelectron spectroscopy. *J. Vac. Sci. Technol.* **2021**, *39*, 060802.
59. Martins, H.P.; Khan, S.A.; Conti, G.; et al. Standing-wave X-ray photoelectron spectroscopy of buried interfaces. *arXiv* **2020**, arXiv:2012.07993.
60. Kobayashi, K.; Yabashi, M.; Takata, Y.; et al. High-resolution, high-energy x-ray photoelectron spectroscopy using third-generation synchrotron radiation source, and its application to Si–high-k insulator systems. *Appl. Phys. Lett.* **2003**, *83*, 1005–1007;
61. Ueda, S.; Katsuya, Y.; Tanaka, M.; et al. Present status of the NIMS contract beamline BL15XU at SPring-8. *AIP Conf. Proc.* **2010**, *1234*, 403–406.
62. Shirley, D.A. High-Resolution X-ray Photoemission Spectrum of the Valence Bands of Gold. *Phys. Rev. B* **1972**, *5*, 4709–4714.
63. Herrera-Gomez, A.; Guzman-Bucio, D.; Cabrera-German, D.; et al. Characterizing the Intrinsic Background in XPS Using the Narrow-Shirley Approach. *J. Phys. Chem. C* **2025**, *129*, 22624–22641.
64. KolXPD, Version 1.8, Kolibrik.net, s.r.o., Žďár nad Sázavou, Czech Republic. Available online: https://www.kolibrik.net/en/solutions-products/kolxpd https (accessed on 26 April 2026).
65. Guo, E.-J.; Gutierrez, M.R.; Sang, X.; et al. Influence of chemical composition and crystallographic orientation on the interfacial magnetism in $BiFeO_3/La_{1-x}Sr_xMnO_3$ superlattices. *Phys. Rev. Mater.* **2018**, *2*, 114404.
66. Korringa, J. On the calculation of the energy of a Bloch wave in a metal. *Physica* **1947**, *13*, 392–400.
67. Ebert, H.; Ködderitzsch, D.; Minár, J. Calculating condensed matter properties using the KKR–Green's function method: Recent developments and applications. *Rep. Prog. Phys.* **2011**, *74*, 096501.
68. De Simone, D.; Vesters, Y.; Vandenberghe, G. Photoresists in extreme ultraviolet lithography (EUVL). *Adv. Opt. Technol.* **2017**, *6*, 163–172.
69. Kostko, O.; Xu, B.; Ahmed, M.; et al. Fundamental understanding of chemical processes in extreme ultraviolet resist materials. *J. Chem. Phys.* **2018**, *149*, 154305.
70. Martins, H.P.; Conti, G.; Cordova, I.; et al. Near total reflection x-ray photoelectron spectroscopy: Quantifying chemistry at solid/liquid and solid/solid interfaces. *J. Phys. D Appl. Phys.* **2021**, *54*, 464002.
71. Ito, H. Chemically amplified resists: Past, present, and future. *Proc. SPIE* **1999**, *3678*, 2–12.
72. Ober, C.K.; Käfer, F.; Yuan, C. Recent developments in photoresists for extreme-ultraviolet lithography. *Polymer* **2023**, *280*, 126020.
73. Kersell, H.; Chen, P.; Martins, H.P.; et al. Simultaneous ambient pressure X-ray photoelectron spectroscopy and grazing incidence X-ray scattering in gas environments. *Rev. Sci. Instrum.* **2021**, *92*, 044102. https://doi.org/10.1063/5.0044162.